Diverse solid and supersolid phases of bosons in a triangular lattice*

Chen Qi-Hui(陈起辉) and Li Peng(李 鹏)†

The Key Laboratory of High Energy Density Physics and Technology of Ministry of Education, College of Physical Science and Technology, Sichuan University, Chengdu 610064, *China*

(Received 12 September 2013; revised manuscript received 14 November 2013; published online 25 March 2014)

We investigate the ground state of bosons with long-range interactions in the large U limit on a triangular lattice. By mapping this system to the spin-1/2 XXZ model in a magnetic field, we can apply the spin wave theory to this study. We demonstrate how to construct the phase diagrams within the spin wave theory. The phase diagrams are given in an extensive parameter region, where, besides the superfluid phase, diverse solid and supersolid phases are shown to exist in this model. Especially, we find that the phase diagram obtained in this method is consistent with the one obtained previously using numerical techniques in the Ising limit. This confirms the effectiveness of our method. We analyze the stability of all the obtained supersolids and show that they will not be ruined by the quantum fluctuations. We observe that the quantum fluctuations in the stripe supersolid phase could be enhanced by the external field. We also discuss the relevance of our result with the experiment that may be realized with ultracold bosonic polar molecules in a triangular optical lattice.

Keywords: supersolid, dipolar molecules, optical lattice

PACS: 67.80.kb, 37.10.Jk, 05.30.Jp **DOI:** 10.1088/1674-1056/23/5/056701

1. Introduction

The investigations of cold atoms and molecules in optical lattices are interesting because we can work on the problems traditionally encountered in condensed matter physics and solid-state physics in a new setting where a high degree of control is possible. Due to the advances of experimental techniques, there is even the possibility to investigate, with appropriately designed atomic systems, intriguing phenomena which do not exist in solid-state materials. Much progress in both experimental and theoretical aspects has been made in the past few decades.[1–7] Various types of optical lattices with interesting geometric structures, such as triangular, kagome, and honeycomb lattices,[8–10] could be realized by the potentials formed by lasers. Furthermore, the interactions between atoms can be tuned by the Feshbach resonance.[11] The Bose–Hubbard model, serving as an explicit example of these quantum systems, has been extensively investigated by using many techniques. The quantum phase transition from superfluid to Mott insulator, which is embedded in the Bose–Hubbard model, has been observed with the aid of ultracold gas in optical lattices.[1]

With the significant experimental progress made in recent years in the cooling and trapping of polar molecules and atomic species having large magnetic moments,[12–14,18] the long-range dipole–dipole interaction has attracted more and more attention.[15–17] Compared with the short-range contact interaction, the long-range interaction could introduce new physical effects, such as geometrical frustration, density-density correlations, and so on. Besides the long-range dipole–dipole interaction, even a variable-range interaction can be generated by applying off-resonant spin-dependent optical dipole forces in experiments.[19]

Motivated by the recent progress in experiments of cold atoms and molecules, we investigate the bosons with long-range interaction in a triangular lattice in this paper. It is well known that the long-range interaction can produce strong frustration in a triangular lattice. The previous study showed that a stable supersolid phase can emerge in this system due to the order by disorder mechanism.[20–25] By considering the long-range interaction, we show that diverse solid and supersolid phases could be realized in such a system. In a lattice system, since the position of each particle is restricted to the lattice site, the solid order, i.e., the diagonal long-range order, is defined as the one that breaks the translational symmetry of the original lattice, while the superfluid order breaks the U(1) symmetry and corresponds to an off-diagonal long-range order. If both orders develop at the same time, then we obtain a supersolid. The supersolid is one of the intriguing exotic phases of matter, of which research works have been carried out in both experimental and theoretical aspects.[26–31] We will discuss in detail how to construct the phase diagram by analyzing the spin wave energy spectrum. By the analysis of the quantum fluctuations on the spin waves, we conclude that all the phases obtained in this system are stable. Finally, we give an experimental protocol for the observations of these phases with bosonic polar molecules in a triangular optical lattice.

This paper is organized as follows. In Section 2, we introduce the model Hamiltonian. In Section 3, we construct

*Project supported by the National Natural Science Foundation of China (Grant No. 11074177) and the Scientific Research Foundation for the Returned Overseas Chinese Scholars of the Ministry of Education, China (Grant No. 20111139-10-2).

†Corresponding author. E-mail: lipeng@scu.edu.cn

© 2014 Chinese Physical Society and IOP Publishing Ltd

the mean field phase diagrams in the large-S limit. In Section 4, we discuss the application of the spin wave theory and give the analysis of quantum fluctuations, phase stability, and excitations. In Section 5, we discuss the relevance of our results with the experiment that might be realized with ultracold bosonic polar molecules in a triangular optical lattice. Finally, we give a brief summary in Section 6.

2. Model Hamiltonian

The general Bose–Hubbard Hamiltonian with long-range interactions in a triangular lattice can be written as

$$H = -t\sum_{\langle ij\rangle} a_i^{\dagger}a_j + \sum_i \left[\frac{1}{2}Un_i(n_i-1) - \mu n_i\right] + \sum_{i,j}\frac{1}{2}V_{ij}n_in_j, \quad (1)$$

where $a_i^{\dagger}$ (a_i) creates (destroys) a boson on site i, $n_i = a_i^{\dagger}a_i$ is the particle number operator, t denotes the nearest neighbor (NN) hopping strength, $\langle ij\rangle$ means the summation over all NN pairs, U is the on-site repulsion and the hard-core constraint $U\to\infty$ is required in this paper, μ is the chemical potential, and V_{ij} is the interaction strength between sites i and j. We will only consider NN interaction V_1 and next nearest neighbor (NNN) interaction V_2 for simplicity. By mapping the empty and the one-particle states to the spin-up and the spin-down states respectively,[32] Hamiltonian (1) can be formulated in a spin $S = 1/2$ representation as

$$H = \sum_{\langle ij\rangle}[-J_x(S_i^xS_j^x + S_i^yS_j^y) + J_zS_i^zS_j^z] + \sum_{(ij)}J_z'S_i^zS_j^z - Sh\sum_i S_i^z, \quad (2)$$

where S_i^{α} is the α component. Here, $J_x = 2t$ and $J_z = V_1$ ($J_z' = V_2$) are the transverse and the longitudinal exchange interactions, respectively, $Sh = \mu + 3V_1 + 3V_2$ is the strength of the external magnetic field, and (ij) means the summation over all NNN pairs. From now on, we take the NN repulsive interaction J_z as the energy unit, i.e., $J_z = 1$, and adopt the parameters $J = J_x/J_z$ ($J \geq 0$) and $\delta = J_z'/J_z$ ($0 \leq \delta \leq 1$).

3. The ground state phase diagrams

In this section, we work out the ground state phase diagram by comparing the energies of different phases in the large-S limit. The analysis of quantum fluctuations, stability, and excitations within the full spin wave theory, i.e., the Holstein–Primakoff approach with large-S expansion, will be presented in the next section. Here several sublattice schemes are designed to capture all the possible interesting phases at the classical level. The sublattice schemes with the corresponding first Brillouin zones (1st BZ) are depicted in Fig. 1. Each classical spin with magnitude S is described by two parameters, the polar and azimuthal angles (θ, ϕ). Since the system is invariant under the global rotation along the z axis and the couplings in the x–y plane are ferromagnetic, we can set $\phi = 0$ without loss of generality. The expressions of the ground state energies for sublattice schemes A, AB, ABC, ABCD are worked out and can be found in Appendix A, from which the phase diagram can be constructed as shown in Figs. 2 and 3. In the spin language, the supersolid order is present when the spins have their x–y components aligned ferromagnetically and their z components ordered at a nonzero wave vector inside the first Brillouin zone.

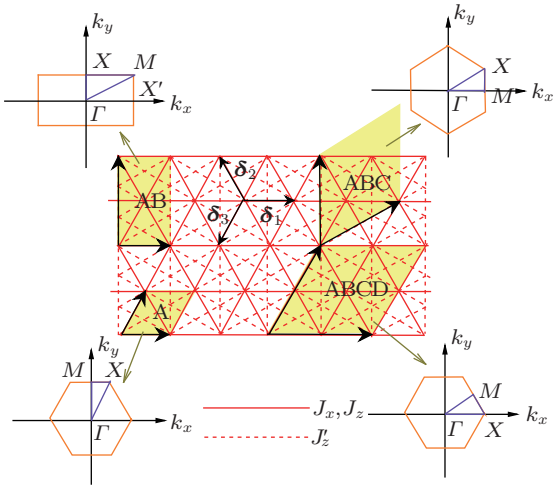


Fig. 1. (color online) The triangular lattice with lattice constant $a = 1$ and four types of sublattice schemes labeled with A, AB, ABC, ABCD and their corresponding first Brillouin zones. The nearest neighbor interactions are denoted by thick red solid lines, and the next nearest neighbor interactions are denoted by thin dashed lines. The lattice translational vectors are $\boldsymbol{\delta}_1 = \{1,0\}$, $\boldsymbol{\delta}_2 = \{-1/2, \sqrt{3}/2\}$, and $\boldsymbol{\delta}_3 = \{-1/2, -\sqrt{3}/2\}$.

3.1. The phase diagram for $J_x = 0$

Because of the particle–hole symmetry, we only need to consider $h > 0$. For the case of $J_x = 0$, the phase diagram is depicted in Fig. 2. It is also worth pointing out that these results are consistent with those obtained by numerical methods.[33] There are four types of emerging diagonal orders, the full occupied Mott phase (full), the stripe solid (stripe-S), the honeycomb solid (honeycomb-S), and the kagome solid (kagome-S), corresponding to the sublattice schemes A, AB, ABC, and ABCD, respectively. The phase transitions between these phases are of first order. We can easily work out analytically the phase boundaries, they are $h_{\rm SH} = 12\delta$ ($0 < \delta \leq 0.2$) between stripe-S and honeycomb-S phases, $h_{\rm SK} = 2(1+\delta)$ ($0.2 < \delta \leq 1$) between stripe-S and kagome-S phases, $h_{\rm HK} = 6 - 18\delta$ ($0 < \delta \leq 0.2$) between honeycomb-S and kagome-S phases, and $h_{\rm KM} = 6(1+\delta)$ ($0 < \delta \leq 1$) between kagome-S and Mott phases. It should be noted that the kagome-S phase will disappear at $\delta = 0$, which is consistent with the previous result.[20]

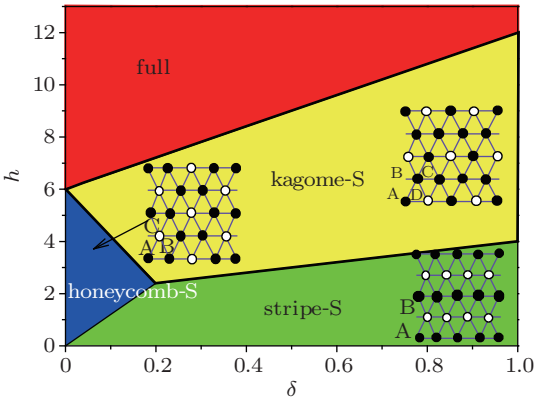


Fig. 2. (color online) The ground state phase diagram in the h–δ plane at $J_x = 0$. The inserted figures show the configurations of solid orders. The solution of polar angle θ on a site is denoted by a black filled circle ($\theta = \pi$) or a white one ($\theta = 0$). All the phase boundaries are of the first order and denoted by black solid lines.

3.2. The phase diagram for $J_x \neq 0$

By fixing δ, we worked out the phase diagrams on the J_x–h plane as depicted in Figs. 3(a) and 3(b). First of all, the superfluid (SF) phase emerges for nonzero J_x. The SF state breaks the global U(1) symmetry with respect to the rotation about the z axis with a uniform polar angle $\theta = \arccos h/[6(1+J_x+\delta)]$ for all lattice sites, i.e., the SF phase is captured by sublattice scheme A. More significantly, several fascinating supersolid phases emerge, including stripe supersolid (stripe-SS), honeycomb supersolid (honeycomb-SS), and kagome supersolid (kagome-SS) phases, due to the coexistence of superfluidity and the corresponding solid orders.

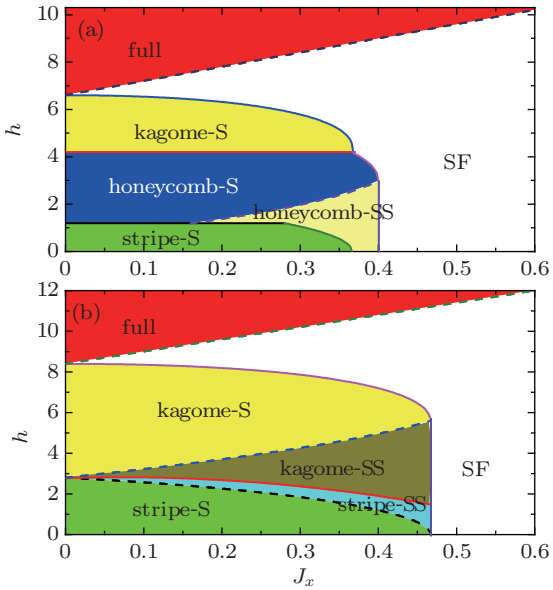


Fig. 3. (color online) The ground state phase diagrams for (a) $\delta = 0.1$ and (b) $\delta = 0.4$ in the J_x–h plane. The first- and the second-order phase transitions at the boundaries are indicated by dashed and solid lines, respectively.

By fixing parameter J_x, we can obtain the numerical solutions of the polar angles of the sublattice sites (θ_α) varying with the applied field as shown in Figs. 4(a) and 4(b). The first- and the second-order phase transitions can be easily observed.

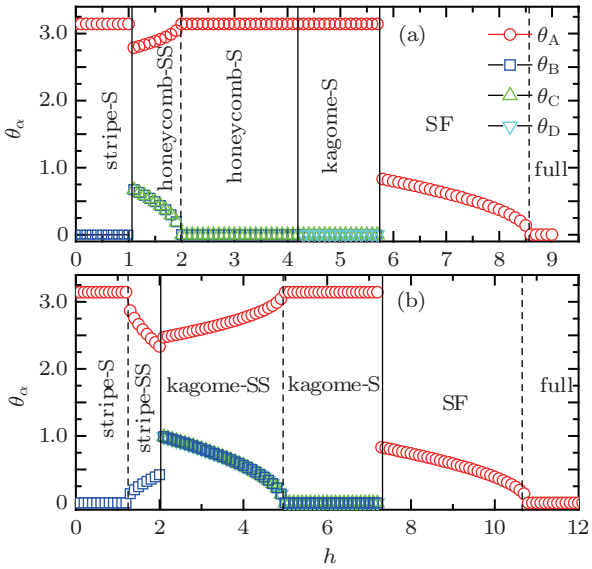


Fig. 4. (color online) The solutions of polar angles θ_α (α = A, B, C, ...) as functions of applied field h with model parameters: (a) $\delta = 0.1$ and $J_x = 0.3$; (b) $\delta = 0.4$ and $J_x = 0.4$. The solid and dashed vertical lines denote the first- and the second-order phase transitions, respectively. The appropriate sublattice scheme is AB for the stripe-S phase, so the sublattice polar angles θ_C and θ_D do not appear; θ_D does not appear for scheme ABC likewise.

Let us discuss the results shown in Fig. 4(a) (i.e., $\delta = 0.1$ and $J_x = 0.3$) first. The system is in the stripe-S phase with $\theta_A = \pi$ and $\theta_B = 0$ when the field h is small. When h exceeds the boundary denoted by

$$h_1 = 2\sqrt{(1+\delta+J_x)(1+\delta-3J_x)}, \tag{3}$$

the system will enter into the honeycomb-SS phase via a first-order phase transition. The appropriate sublattice scheme changes from AB to ABC. The sublattice polar angles θ_A, θ_B, and θ_C take incommensurate values. Notice that this supersolid phase is absent for

$$J_x < J_x^{c1} = \left[3\delta - 1 + \sqrt{(1-3\delta)(1+5\delta)}\right]/2. \tag{4}$$

When h reaches the second-order transition boundary

$$h_2 = \frac{3}{2}\left(2 + J_x - \sqrt{4(1-2\delta)(1-2\delta-4J_x) - 7J_x^2}\right), \tag{5}$$

a honeycomb-S phase with commensurate polar angles $\theta_A = \pi$ and $\theta_B = \theta_C = 0$ develops due to the disappearance of the superfluid density. If h further exceeds

$$h_3 = 6(1-3\delta), \tag{6}$$

the system enters into the kagome-S phase through a first-order phase transition. Again, the appropriate sublattice scheme changes from ABC to ABCD. In the kagome-S phase, we have $\theta_A = \pi$ and $\theta_B = \theta_C = \theta_D = 0$. The next phase boundary

$$h_4 = 3\left(1 + J_x + \delta + \sqrt{(1+\delta-3J_x)(1+\delta+J_x)}\right) \tag{7}$$

is of the first order, which separates the kagome-S phase from the SF phase. Eventually, when h exceeds the boundary

$$h_5 = 6(1+J_x+\delta), \tag{8}$$

the system enters into in the Mott insulator phase with each site being fully occupied by one boson.

The discussion for Fig. 4(b) (i.e., $\delta = 0.4$ and $J_x = 0.4$) could be carried out in the same way. In this case, the honeycomb configurations do not appear at all. With h increasing, the system goes through the stripe-S, stripe-SS, kagome-SS, kagome-S, SF, and Mott phases successively, with phase boundaries (only h_2' separating the stripe and the kagome supersolid phases needs to be solved numerically)

$$h_1' = 2\sqrt{(1+\delta+J_x)(1+\delta-3J_x)}, \tag{9}$$

$$h_3' = 2\left(2+J_x+2\delta-\sqrt{(1+\delta)(1+\delta-2J_x)-2J_x^2}\right), \tag{10}$$

$$h_4' = 3\left(1+J_x+\delta+\sqrt{(1+\delta-3J_x)(1+\delta+J_x)}\right), \tag{11}$$

$$h_5' = 6(1+J_x+\delta). \tag{12}$$

4. Spin wave theory: the Holstein–Primakoff approach

Now we apply the full spin wave theory (SWT) to the problem by emphasizing the quantum fluctuations and excitations. Without loss of generality, we suppose that the whole lattice is divided into M sublattices denoted by $\nu = 1,2,\ldots,M$. Just as we have done in the previous section, we can work out the mean-field ground state that is characterized by the polar angle θ_ν for the ν-th sublattice. Then we perform a local rotation so that the direction of the local spin points to the local quantization z axis. Since all spins are assumed to lie in the x–z plane, we can do this by a rotation about the y axis. By labeling the local frame with a tilde, we obtain the transformation

$$\begin{aligned} S^x_{\boldsymbol{R},\nu} &= \cos\theta_\nu \tilde{S}^x_{\boldsymbol{R},\nu} + \sin\theta_\nu \tilde{S}^z_{\boldsymbol{R},\nu}, \\ S^y_{\boldsymbol{R},\nu} &= \tilde{S}^y_{\boldsymbol{R},\nu}, \\ S^z_{\boldsymbol{R},\nu} &= -\sin\theta_\nu \tilde{S}^x_{\boldsymbol{R},\nu} + \cos\theta_\nu \tilde{S}^z_{\boldsymbol{R},\nu}, \end{aligned} \tag{13}$$

where the subscript $\boldsymbol{R}$ labels a Bravais lattice site.

We introduce M bosonic annihilation operators, d_ν ($\nu = 1,2,\ldots,M$), and their corresponding creation operators. By means of the Holstein–Primakoff transformation, we can represent the spins on sublattice ν as follows:

$$\begin{aligned} \tilde{S}^+_{\boldsymbol{R},\nu} &= d^\dagger_{\boldsymbol{R},\nu}\sqrt{2S-n_{\boldsymbol{R},\nu}} = \sqrt{2S}d^\dagger_{\boldsymbol{R},\nu} + \mathcal{O}(S^{-\frac{1}{2}}), \\ \tilde{S}^-_{\boldsymbol{R},\nu} &= \sqrt{2S-n_{\boldsymbol{R},\nu}}d_{\boldsymbol{R},\nu} = \sqrt{2S}d_{\boldsymbol{R},\nu} + \mathcal{O}(S^{-\frac{1}{2}}), \\ \tilde{S}^z_{\boldsymbol{R},\nu} &= S - d^\dagger_{\boldsymbol{R},\nu}d_{\boldsymbol{R},\nu} = S - n_{\boldsymbol{R},\nu}, \end{aligned} \tag{14}$$

where $\boldsymbol{R} \in \nu$ sublattice, $n_{\boldsymbol{R},\nu} = d^\dagger_{\boldsymbol{R},\nu}d_{\boldsymbol{R},\nu}$ is the particle number operator, and $S^\pm_{\boldsymbol{R},\nu} = \tilde{S}^x_{\boldsymbol{R},\nu} \pm \mathrm{i}\tilde{S}^y_{\boldsymbol{R},\nu}$. By substituting Eqs. (13) and (14) in Hamiltonian (2) and performing the Fourier transformation, we can write the Hamiltonian in the form

$$H = \mathcal{H}_0 + \mathcal{H}_1 + \mathcal{O}(S^0), \tag{15}$$

where $\mathcal{H}_0$ is the classical mean-field ground state energy (just as the ones listed in Appendix A, Eqs. (A1)–(A3)) that is proportional to S^2. The $\mathcal{H}_1$ is the leading-order quantum fluctuation proportional to S with the explicit form

$$\mathcal{H}_1 = \frac{1}{2}S\sum_{\boldsymbol{k}}\left(\boldsymbol{A}^\dagger(\boldsymbol{k}), \tilde{\boldsymbol{A}}(\boldsymbol{k})\right)\begin{pmatrix}\mathcal{M} & \mathcal{N}\\ \mathcal{N} & \mathcal{M}\end{pmatrix}\begin{pmatrix}\boldsymbol{A}(\boldsymbol{k})\\ \tilde{\boldsymbol{A}}^\dagger(\boldsymbol{k})\end{pmatrix} + E^0_{\mathrm{FL}}, \tag{16}$$

where $\boldsymbol{A}^\dagger(\boldsymbol{k}) = (d_1^\dagger(\boldsymbol{k}), d_2^\dagger(\boldsymbol{k}), \ldots, d_M^\dagger(\boldsymbol{k}))$, $\tilde{\boldsymbol{A}}$ is the transpose of $\boldsymbol{A}$, from which we can define the spinor $\boldsymbol{D}^\dagger(\boldsymbol{k}) = (\boldsymbol{A}^\dagger(\boldsymbol{k}), \tilde{\boldsymbol{A}}(\boldsymbol{k}))$, $\mathcal{M}$ and $\mathcal{N}$ are $M\times M$ matrices (see Appendix B), and E^0_{FL} is a constant in S order. The $\mathcal{H}_1$ can be diagonalized by using the extended Bogoliubov transformation, which amounts to finding a rank $2M\times 2M$ matrix $\boldsymbol{U}$ satisfying

$$\boldsymbol{U}^\dagger\boldsymbol{\Lambda}\boldsymbol{U} = \boldsymbol{\Lambda}, \tag{17}$$

$$\boldsymbol{U}^\dagger\mathcal{H}_1\boldsymbol{U} = \boldsymbol{\Omega}, \tag{18}$$

with

$$\boldsymbol{\Lambda} = \begin{pmatrix}\mathbf{1} & 0\\ 0 & -\mathbf{1}\end{pmatrix}, \qquad \boldsymbol{\Omega} = \begin{pmatrix}\boldsymbol{\omega}(\boldsymbol{k}) & 0\\ 0 & \boldsymbol{\omega}(-\boldsymbol{k})\end{pmatrix}, \tag{19}$$

where $\mathbf{1}$ is an identity matrix of size M, and $\boldsymbol{\omega}(\boldsymbol{k})$ is a diagonal matrix, i.e., $\boldsymbol{\omega}(\boldsymbol{k}) = \mathrm{diag}(\omega_1(\boldsymbol{k}), \omega_2(\boldsymbol{k}), \ldots, \omega_M(\boldsymbol{k}))$. Equation (17) is a condition that ensures the statistics of the system, i.e., the system will remain bosonic natured after the transformation. Equation (18) ensures the diagonalization of the Hamiltonian, which is just a mathematical requirement. The transformation matrix $\boldsymbol{U}$ and energy spectrum matrix $\boldsymbol{\Omega}$ can be obtained by solving the following matrix equation:

$$\boldsymbol{\Lambda}\mathcal{H}_1\boldsymbol{U} = \boldsymbol{U}\boldsymbol{\Lambda}\boldsymbol{\Omega}, \tag{20}$$

which can be inferred from Eqs. (17) and (18).

We introduce another set of bosonic operators $\alpha_\nu(\boldsymbol{k})$ ($\nu = 1,2,\ldots,M$) and spinor $\mathcal{D}^\dagger(\boldsymbol{k}) = (\mathcal{A}^\dagger(\boldsymbol{k}), \tilde{\mathcal{A}}(-\boldsymbol{k}))$ with $\mathcal{A}^\dagger(\boldsymbol{k}) = (\alpha_1^\dagger(\boldsymbol{k}), \alpha_2^\dagger(\boldsymbol{k}), \ldots, \alpha_M^\dagger(\boldsymbol{k}))$. We suppose that $\mathcal{H}_1$ is diagonal in terms of these new bosons (i.e., $\mathcal{D}(\boldsymbol{k}) = \boldsymbol{U}^{-1}\boldsymbol{D}(\boldsymbol{k})$),

$$\mathcal{H}_1 = S\sum_{\nu,\boldsymbol{k}}\omega_\nu(\boldsymbol{k})[\alpha_\nu^\dagger(\boldsymbol{k})\alpha_\nu(\boldsymbol{k}) + 1/2] + E^0_{\mathrm{FL}}. \tag{21}$$

So the total spin-wave correction to the ground-state energy reads

$$\Delta E = \frac{1}{2}S\sum_{\nu,\boldsymbol{k}}\omega_\nu(\boldsymbol{k}) + E^0_{\mathrm{FL}}. \tag{22}$$

4.1. Revisit the ground state phase diagram with spin waves

In Section 3, we have presented the ground state phase diagram in the classical large-S limit. Now we discuss how those sublattice schemes can be reproduced from the spin wave analysis and whether the phases are stable or not when quantum fluctuations are included. We can easily work out the ground states of the system in two limiting cases. One is when h is large enough, the system is in the full occupied Mott insulator phase. This case is trivial for our discussion. The other is when J_x is large enough, the system is in the superfluid phase. In the SF regime, we can work out the energy spectrum with sublattice scheme A (see Fig. 1) and obtain the analytical result

$$\omega_{\rm A}(\boldsymbol{k}) = \sqrt{\mathcal{M}_{\rm A}(\boldsymbol{k})^2 - \mathcal{N}_{\rm A}(\boldsymbol{k})^2}, \tag{23}$$

where $\mathcal{M}_{\rm A}(\boldsymbol{k})$ and $\mathcal{N}_{\rm A}(\boldsymbol{k})$ are given by Eqs. (B1) and Eq. (B2), respectively, in Appendix B. In the SF phase, the spectrum exhibits a gapless mode at Γ $(0,\ 0)$ point in the 1st BZ (see sublattice scheme A in Fig. 1). We now show that the emergent phases with stripe and honeycomb solid orders (i.e., the sublattice schemes AB and ABC are needed accordingly) are actually embedded in the spectrum given by Eq. (23). This can be inferred from the gapless behavior of the spectrum, because the Bose condensation occurs for the Holstein–Primakoff bosons and leads to the particular solid order. Numerical solutions of the spectrum are shown in Fig. 5 for several selected parameters. We analyze the behavior of the spectrum when J_x reduces away from the superfluid regime. In the 1st BZ, a minimum (usually called a "roton") at M $(0,\ 2\pi/\sqrt{3})$ or X $(2\pi/3,\ 2\pi/\sqrt{3})$ point develops as J_x decreases. At the transition value J_x^{c2}, the minimum becomes a gapless Goldstone mode (i.e., the roton is totally softened). If the softened mode occurs at the M point, then the stripe order with sublattice scheme AB appears; while if the softened mode occurs at the X point, then the honeycomb order with sublattice scheme ABC appears. This is in agreement with the phase diagrams, Figs. 2 and 3, established in the previous section.

We notice that the phases with sublattice scheme ABCD are not embedded in the spectrum given by Eq. (23). This is not hard to understand since the kagome order cannot be represented by a faithful single mode in the 1st BZ of sublattice scheme A. So we resort to sublattice scheme AB. Since there are two sublattices, we have two branches of spectra labeled by $\omega_{\rm A}(\boldsymbol{k})$ and $\omega_{\rm B}(\boldsymbol{k})$. They can be numerically solved from Eq. (20). The result is shown in Fig. 6. We see that the softened roton develops at the M $(\pi,\ \pi/\sqrt{3})$ point (see the 1st BZ of sublattice scheme AB in Fig. 1 for both spectra). When gaplessness occurs at the M point, the Bose condensation of Holstein–Primakoff bosons leads to kagome orders with sublattice scheme ABCD eventually.

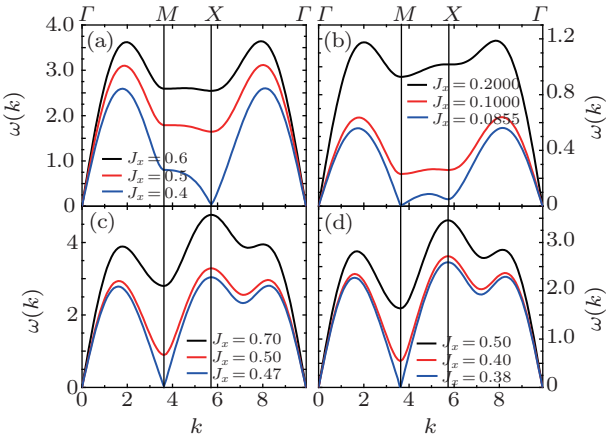


Fig. 5. (color online) The energy spectrum obtained with Eq. (23). The selected parameters are (a) $\delta = 0.1$ and $h = 0.1$; (b) $\delta = 0.1$ and $h = 6$; (c) $\delta = 0.4$ and $h = 0.1$; (d) $\delta = 0.4$ and $h = 4$. From the roton mode at the M or X point, we can infer the formation of the stripe or honeycomb order.

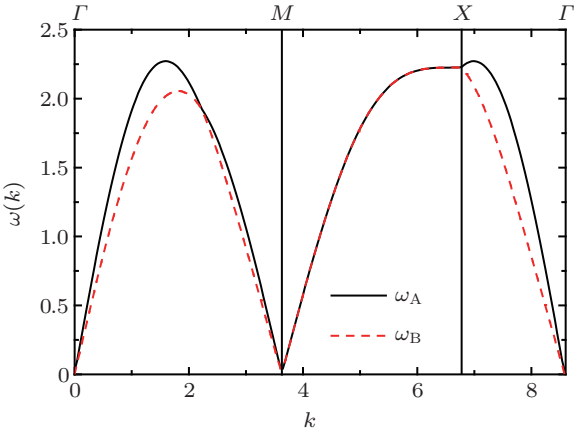


Fig. 6. (color online) The numerical solution of energy spectrum for sublattice scheme AB (see Fig. 1) with parameters $K_z = 0.4$, $h = 4$, and $J_x = 0.38365$. We observe a softened roton at the M point. When it becomes gapless, a kagome order will develop.

Next, we discuss the properties of excitations in different phases. In Fig. 7(a), we show the energy spectra in the SF phase with different parameters. We find that the excitation is always gapless and linear in k at the long wavelength limit (at the Γ point), which is consistent with the Goldstone theorem. In Figs. 7(b)–7(d), we show the spectra for sublattice schemes AB, ABC, and ABCD respectively, which display clear transitions from the stripe-, honeycomb-, and kagome-SS phases to the stripe-, honeycomb-, and kagome-S phases, respectively. At the supersolid–solid transition point, the gapless spectra change their behaviors from linear ($\simeq k$) to quadratic ($\simeq k^2$). While in the solid phases, the spectra are gapped. The total energies (including spin-wave corrections) in the solid phases are independent of h, which demonstrates their incompressibility due to the solid order.

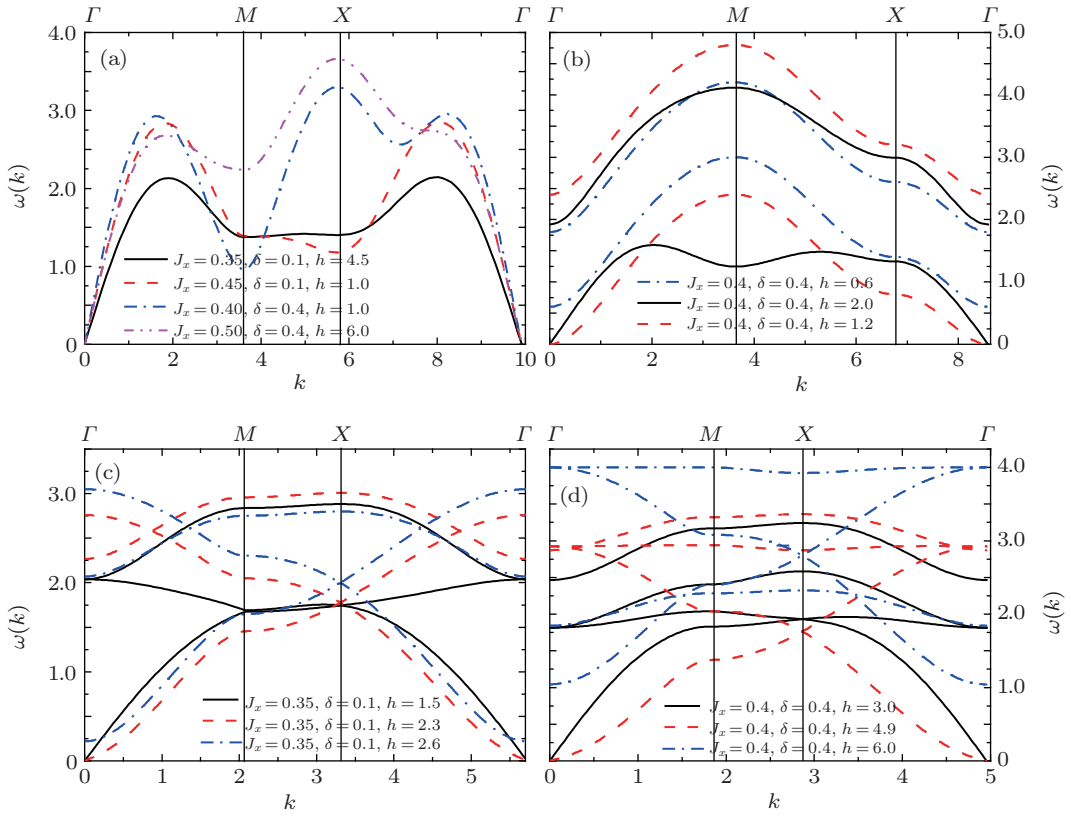


Fig. 7. (color online) The energy spectra for different sublattice schemes and the number of branches: (a) scheme A for SF phase, 1 branch; (b) scheme AB for stripe-SS and stripe-S phases, 2 branches; (c) scheme ABC for honeycomb-SS and honeycomb-S phases, 3 branches; (d) scheme ABCD for kagome-SS and kagome-S phases, 4 branches. The black solid lines are for the supersolid phases. The red dashed lines are for the supersolid–solid transitions. The blue dash-dotted lines are for the solid phases.

4.2. Quantum fluctuations

Finally, we turn to the quantum fluctuations that might destroy the orders of the mean-field ground states. The magnetization in sublattice ν ($\nu = 1, 2, \ldots, M$) is defined as the average of the spin component along its quantization axis

$$\langle \tilde{S}^z_\nu \rangle = \frac{1}{N} \sum_{i \in \nu} \langle \tilde{S}^z_i \rangle = S - \Delta \tilde{S}^z_\nu, \tag{24}$$

where S is the classical value of the spin, and N is the number of ν sublattice sites. The second term $\Delta \tilde{S}^z_\nu$ is the reduction from the classical value of the spin due to the quantum fluctuations. The $\langle Q \rangle$ is the expectation value of operator Q in the ground state. Here $\Delta \tilde{S}^z_\nu$ can be calculated from the Bogoliubov transformation matrix $\boldsymbol{U}(\boldsymbol{k})$

$$\begin{aligned} \Delta \tilde{S}^z_\nu &= \frac{1}{N} \sum_{i \in \nu} \langle d^\dagger_i d_i \rangle = \frac{1}{N} \sum_{\boldsymbol{k}} \langle d^\dagger_{\boldsymbol{k}} d_{\boldsymbol{k}} \rangle \\ &= \frac{1}{N} \sum_{\boldsymbol{k}} \sum_{l=M+1}^{2M} |U_{\nu l}(\boldsymbol{k})|^2, \end{aligned} \tag{25}$$

where $\boldsymbol{U}(\boldsymbol{k})$ is obtained by solving Eq. (20). Particularly, we can work it out analytically for sublattice scheme A as follows:

$$U_{12}(\boldsymbol{k}) = \frac{\mathcal{M}_{\mathrm{A}}(\boldsymbol{k}) - \omega_{\mathrm{A}}(\boldsymbol{k})}{2\omega_{\mathrm{A}}(\boldsymbol{k})}.$$

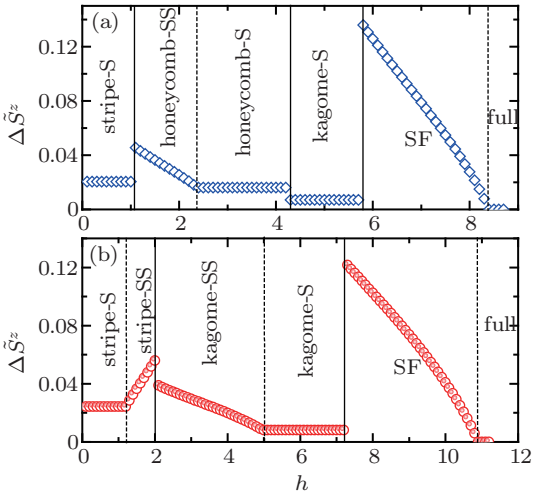


Fig. 8. (color online) The quantum fluctuations to the magnetization, $\Delta \tilde{S}^z$, as a function of external field h, where the parameters in panels (a) and (b) are the same as those in Figs. 4(a) and 4(b), respectively.

For other sublattice schemes, the fluctuations can be calculated in the same way. In this paper, we use $\Delta \tilde{S}^z = (1/M) \sum_\nu \Delta \tilde{S}^z_\mu$ to measure the strength of the quantum fluctuation for abbreviation. The results of $\Delta \tilde{S}^z$ are shown in Fig. 8. We can see that the quantum fluctuation is not strong enough to destroy the orders in the solid and the supersolid phases. Especially, ΔS^z is always a small constant in the solid phases. In the superfluid phase, the fluctuations can grow up slightly,

however it is still not very strong. It is noteworthy that all types of supersolids are stable. This conclusion is consistent with the one given by others.[16] We observe an interesting phenomenon, betraying one's intuition, that the external field can somehow enhance rather than suppress the quantum fluctuations in the stripe-SS phase (Fig. 8(b)). This could be reasonably attributed to the frustration induced by the triangular geometry.[34]

5. Experimental protocol

The long-range interaction in some parameter regions considered here can be realized using bosonic polar molecules in triangular optical lattices. We can consider heteronuclear molecules, such as SrO with a permanent dipole moment of $d \approx 8.9$ D or LiCs with a dipole moment of $d \approx 6.3$ D, which are relevant in the present experiments,[35–38] prepared in their electronic and vibrational ground states. The polar molecules are trapped in the xy plane by a standing wave laser, which is formed by two counter-propagating laser beams with $\omega_\perp \approx 9.42 \times 10^4$ Hz. The triangular optical lattices can be set up by three laser beams of $\lambda \approx 940$ nm for LiCs in the xy plane with a $2\pi/3$ angle between each other.[39] To obtain an isotropic dipole–dipole interaction, a strong DC electric field should be employed along the z direction, which induces the dipole moment along this direction. Integrating over the z direction, eventually, we obtain a long range dipole–dipole interaction as $V_{\rm eff}^{\rm 2D} \sim D/r^3$. For more details, we refer to Refs. [40] and [41]. To identify those phases in the experiment, the standard time-of-flight image technology can be applied as a useful tool.[39] In the superfluid phase, a strong peak will appear at $\boldsymbol{k} = 0$ due to the algebraic decay of the Green function. Different solids and supersolids can be distinguished by different peak structures and different peak strengths in the first Brillouin zone.

6. Summary

Motivated by the realization of cold atoms with long-range dipole interactions, we have investigated the hard-core boson model with long-range interactions on a triangular lattice. By mapping it to the spin-1/2 XXZ model, we applied the spin wave theory in this study. We have constructed the mean field phase diagram, analyzed the low lying excitations, and discussed the phase transitions. We have also considered the quantum fluctuations that may destroy the solid and the supersolid phases and concluded that all the phases found here are stable. Finally, we gave an experimental protocol to realize the phases in some parameter regions. On the other hand, due to the equivalence of the hard-cord boson model and the spin-1/2 XXZ model, the results disclosed here might also be detected in spin systems with long-range diagonal exchange interactions in future experiments.

Appendix A: the mean-field ground state energies

The mean-field ground state energies per site corresponding to those sublattice schemes (see Fig. 1) are

$$\begin{aligned} E_{\rm AB}/S^2 = & \sum_{\alpha={\rm A,B}} \left[-\frac{1}{2}(J_x+\delta+1)\sin^2\theta_\alpha - \frac{h}{2}\cos\theta_\alpha \right] \\ & + 2[(1+\delta)\cos\theta_{\rm A}\cos\theta_{\rm B} - J_x \sin\theta_{\rm A}\sin\theta_{\rm B}] \\ & + (1+\delta), \end{aligned} \tag{A1}$$

$$\begin{aligned} E_{\rm ABC}/S^2 = & \sum_{\alpha={\rm A,B,C}} [\delta\cos^2\theta_\alpha - (h/3)\cos\theta_\alpha] \\ & + \sum_{\langle\alpha,\beta\rangle} [\cos\theta_\alpha\cos\theta_\beta - J_x\sin\theta_\alpha\sin\theta_\beta], \end{aligned} \tag{A2}$$

$$\begin{aligned} E_{\rm ABCD}/S^2 = & \sum_{\langle\alpha,\beta\rangle} [\delta\cos\theta_\alpha\cos\theta_\beta - J_x\sin\theta_\alpha\sin\theta_\beta/2] \\ & - \sum_{\alpha={\rm A,B,C,D}} (h/4)\cos\theta_\alpha, \end{aligned} \tag{A3}$$

where $\langle\alpha,\beta\rangle$ means summation over all the possible pairs of sublattice labels, e.g., $\langle {\rm A,B}\rangle$, $\langle {\rm B,C}\rangle$, and so on. The parameters θ_α are determined by minimization of the mean-field energies.

Appendix B: matrices $\mathcal{M}$ and $\mathcal{N}$

The elements of $\mathcal{M}$ and $\mathcal{N}$ in sublattice scheme A are

$$\begin{aligned} \mathcal{M}_{\rm A}(\boldsymbol{k}) = & h\cos\theta + 6J_x + 6(J_x+\delta+1)\cos^2\theta \\ & + [(1+J_x)\sin^2\theta - 2J_x]\gamma_1(\boldsymbol{k}) \\ & + \delta\gamma_2(\boldsymbol{k})\sin^2\theta, \end{aligned} \tag{B1}$$

$$\mathcal{N}_{\rm A}(\boldsymbol{k}) = (1+J_x)\sin^2\theta\gamma_1(\boldsymbol{k}) + \delta\sin^2\theta\gamma_2(\boldsymbol{k}), \tag{B2}$$

with $\cos\theta = h/(1+J_x+\delta)$, $\gamma_1(\boldsymbol{k}) = \sum_{\alpha=1}^3 \cos(\boldsymbol{k}\cdot\delta_\alpha)$, and $\gamma_2(\boldsymbol{k}) = \sum_{\alpha=1}^3 \cos[\boldsymbol{k}\cdot(\delta_\alpha - \delta_{\alpha-1})]$. For simplicity, we introduce the following notations:

$$\begin{aligned} X^1_{\nu\nu'} &\equiv \cos\theta_\nu\cos\theta_{\nu'} - J_x\sin\theta_\nu\sin\theta_{\nu'}, \\ X^2_{\nu\nu'} &\equiv \delta\cos\theta_\nu\cos\theta_{\nu'}, \\ F^1_{\nu\nu'} &\equiv \frac{1}{2}\left(\sin\theta_\nu\sin\theta_{\nu'} - J_x\cos\theta_\nu\cos\theta_{\nu'} - J_x\right), \\ F^2_{\nu\nu'} &\equiv \frac{1}{2}\left(\delta\sin\theta_\nu\sin\theta_{\nu'}\right), \\ G^1_{\nu\nu'} &\equiv \frac{1}{2}\left(\sin\theta_\nu\sin\theta_{\nu'} - J_x\cos\theta_\nu\cos\theta_{\nu'} + J_x\right), \\ G^2_{\nu\nu'} &\equiv \frac{1}{2}\left(\delta\sin\theta_\nu\sin\theta_{\nu'}\right), \\ h_\nu &\equiv h\cos\theta_\nu\gamma^1_{\nu\nu'} \equiv \sum_\sigma {\rm e}^{-{\rm i}\boldsymbol{k}\cdot\boldsymbol{\delta}^\sigma_{\nu\nu'}}, \quad \gamma^2_{\nu\nu'} \equiv \sum_\sigma {\rm e}^{-{\rm i}\boldsymbol{k}\cdot\boldsymbol{\Delta}^\sigma_{\nu\nu'}}, \end{aligned}$$

where $\boldsymbol{\delta}^\sigma_{\nu\nu'}$ and $\boldsymbol{\Delta}^\sigma_{\nu\nu'}$ are the translational vectors connecting sublattices ν and ν' along direction σ for nearest neighbors and next nearest neighbors, respectively. The matrices $\mathcal{M}$ and $\mathcal{N}$ for sublattice schemes AB, ABC, and ABCD are

$$\mathcal{M}_{\rm AB} = \begin{bmatrix} \Gamma_{\rm AB}(A) & \sum_\mu F^\mu_{\rm AB}\gamma^\mu_{\rm AB} \\ \sum_\mu F^\mu_{\rm AB}\gamma^\mu_{\rm AB} & \Gamma_{\rm AB}(B) \end{bmatrix}, \tag{B3}$$

$$\mathcal{N}_{\rm AB}=\begin{bmatrix}\sum_\mu G^\mu_{\rm AA}\gamma^\mu_{\rm AA} & \sum_\mu G^\mu_{\rm AB}\gamma^\mu_{\rm AB}\\ \sum_\mu G^\mu_{\rm AB}\gamma^\mu_{\rm AB} & \sum_\mu G^\mu_{\rm BB}\gamma^\mu_{\rm BB}\end{bmatrix}, \tag{B4}$$

with

$$\Gamma_{\rm AB}(\rho)=h_\rho-\sum_{\nu,\mu}(z_{\rho\nu}X^\mu_{\rho\nu})+\sum_\mu F^\mu_{\rho\rho}\gamma^\mu_{\rho\rho},$$

$$\mathcal{M}_{\rm ABC}=\begin{bmatrix}\Gamma_{\rm ABC}(A) & F^1_{\rm AB}\gamma^1_{\rm AB} & F^1_{\rm AC}\gamma^1_{\rm AC}\\ F^1_{\rm BA}\gamma^1_{\rm BA} & \Gamma_{\rm ABC}(B) & F^1_{\rm BC}\gamma^1_{\rm BC}\\ F^1_{\rm CA}\gamma^1_{\rm CA} & F^1_{\rm CB}\gamma^1_{\rm CB} & \Gamma_{\rm ABC}(C)\end{bmatrix}, \tag{B5}$$

$$\mathcal{N}_{\rm ABC}=\begin{bmatrix}G^2_{\rm AA}\gamma^2_{\rm AA} & G^1_{\rm AB}\gamma^1_{\rm AB} & G^1_{\rm AC}\gamma^1_{\rm AC}\\ G^1_{\rm BA}\gamma^1_{\rm BA} & G^2_{\rm BB}\gamma^2_{\rm BB} & G^1_{\rm BC}\gamma^1_{\rm BC}\\ G^1_{\rm CA}\gamma^1_{\rm CA} & G^1_{\rm CB}\gamma^1_{\rm CB} & G^2_{\rm CC}\gamma^2_{\rm CC}\end{bmatrix}, \tag{B6}$$

with

$$\Gamma_{\rm ABC}(\rho)=h_\rho+F^2_{\rho\rho}\gamma^2_{\rho\rho}-\sum_{\nu\mu}z_{\rho\nu}X^\mu_{\rho\nu},$$

$$\mathcal{M}_{\rm ABCD}=\begin{bmatrix}\Gamma_{\rm ABCD}(A) & \sum_\mu F^\mu_{\rm AB}\gamma^\mu_{\rm AB} & \sum_\mu F^\mu_{\rm AC}\gamma^\mu_{\rm AC} & \sum_\mu F^\mu_{\rm AD}\gamma^\mu_{\rm AD}\\ \sum_\mu F^\mu_{\rm BA}\gamma^\mu_{\rm BA} & \Gamma_{\rm ABCD}(B) & \sum_\mu F^\mu_{\rm BC}\gamma^\mu_{\rm BC} & \sum_\mu F^\mu_{\rm BD}\gamma^\mu_{\rm BD}\\ \sum_\mu F^\mu_{\rm CA}\gamma^\mu_{\rm CA} & \sum_\mu F^\mu_{\rm CB}\gamma^\mu_{\rm CB} & \Gamma_{\rm ABCD}(C) & \sum_\mu F^\mu_{\rm CD}\gamma^\mu_{\rm CD}\\ \sum_\mu F^\mu_{\rm DA}\gamma^\mu_{\rm DA} & \sum_\mu F^\mu_{\rm DB}\gamma^\mu_{\rm DB} & \sum_\mu F^\mu_{\rm DC}\gamma^\mu_{\rm DC} & \Gamma_{\rm ABCD}(D)\end{bmatrix}, \tag{B7}$$

$$\mathcal{N}_{\rm ABCD}=\begin{bmatrix}0 & \sum_\mu G^\mu_{\rm AB}\gamma^\mu_{\rm AB} & \sum_\mu G^\mu_{\rm AC}\gamma^\mu_{\rm AC} & \sum_\mu G^\mu_{\rm AD}\gamma^\mu_{\rm AD}\\ \sum_\mu G^\mu_{\rm BA}\gamma^\mu_{\rm BA} & 0 & \sum_\mu G^\mu_{\rm BC}\gamma^\mu_{\rm BC} & \sum_\mu G^\mu_{\rm BD}\gamma^\mu_{\rm BD}\\ \sum_\mu G^\mu_{\rm CA}\gamma^\mu_{\rm CA} & \sum_\mu G^\mu_{\rm CB}\gamma^\mu_{\rm CB} & 0 & \sum_\mu G^\mu_{\rm CD}\gamma^\mu_{\rm CD}\\ \sum_\mu G^\mu_{\rm DA}\gamma^\mu_{\rm DA} & \sum_\mu G^\mu_{\rm DB}\gamma^\mu_{\rm DB} & \sum_\mu G^\mu_{\rm DC}\gamma^\mu_{\rm DC} & 0\end{bmatrix}, \tag{B8}$$

with

$$\Gamma_{\rm ABCD}(\rho)h_\rho-\sum_{\nu\mu}z_{\rho\nu}X^\mu_{\rho\nu},$$

respectively, with $\mu(\nu)=1,2$ representing the interactions of nearest neighbors and next nearest neighbors, and $z_{\nu\nu'}$ is the number of sublattice ν connecting with a given site of sublattice ν'.

References

[1] Greiner M, Mandel O, Esslinger T, Hänsch T W and Bloch I 2002 *Nature* **415** 39

[2] Trotzky S, Cheinet P, Fölling S, Feld M, Schnorrberger U, Rey A M, Polkovnikov A, Demler E A, Lukin M D and Bloch I 2008 *Science* **319** 295

[3] Fölling S, Trotzky S, Cheinet P, Feld M, Saers R, Widera A, Müller T and Bloch I 2007 *Nature* **448** 1029

[4] Chen Y A, Nascimbéne S, Aidelsburger M, Atala M, Trotzky S and Bloch I 2011 *Phys. Rev. Lett.* **107** 210405

[5] Sebby-Strabley J, Anderlini M, Jessen P S and Porto J V 2006 *Phys. Rev. A* **73** 033605

[6] Duan L M, Demler E and Lukin M D 2003 *Phys. Rev. Lett.* **91** 090402

[7] Jaksch S, Bruder C, Cirac J I, Gardiner C W and Zoller P 1998 *Phys. Rev. Lett.* **81** 3108

[8] Santos L, Baranov M A, Cirac J I, Everts H U, Fehrmann H and Lewenstein M 2004 *Phys. Rev. Lett.* **93** 030601

[9] Soltan-Panachi P, Struck J, Hauke P, Bick A, Plenkers W, Meineke G, Becker C, Windpassinger P, Lewenstein M and Sengstock K 2011 *Nat. Phy.* **7** 434

[10] Chen Y H, Wu W, Tao H S and Liu W M 2010 *Phys. Rev. A* **82** 043625

[11] Bloch I, Dalibard J and Zwerger W 2008 *Rev. Mod. Phys.* **80** 885

[12] Ni K K, Ospelkaus S, de Miranda M H G, Peer A, Neyenhuis B, Zirbel J J, Kotochigova S, Julienne P S, Jin D S and Ye J 2008 *Science* **322** 231

[13] Deiglmayr J, Grochola A, Repp M, Mörtlbauer K, Glück C, Lange J, Dulieu O, Wester R and Weidemüller M 2008 *Phys. Rev. Lett.* **101** 133004

[14] Griesmaier A, Werner J, Hensler S, Stuhler J and Pfau T 2005 *Phys. Rev. Lett.* **94** 160401

[15] Pollet L, Picon J D, Büchler H P and Troyer M 2010 *Phys. Rev. Lett.* **104** 125302

[16] Yamamoto D, Danshita I and Sá de Melo C A R 2012 *Phys. Rev. A* **85** 021601

[17] Lahaye T, Menotti C, Santos L, Lewenstein M and Pfau T 2009 *Rep. Prog. Phys.* **72** 126401

[18] Zhang Y C, Wang H T, Shen S Q and Liu W M 2013 *Chin. Phys. B* **22** 090501

[19] Islam R, Senko C, Campbell W C, Korenblit S, Smith J, Lee A, Edwards E E, Wang C C J, Freericks J K and Monroe C 2013 *Science* **340** 583

[20] Murthy G, Arovas D and Auerbach A 1997 *Phys. Rev. B* **55** 3104

[21] Melko R G, Paramekanti A, Burkov A A, Vishwanath A, Sheng D N and Balents L 2005 *Phys. Rev. Lett.* **95** 127207

[22] Wessel S and Troyer M 2005 *Phys. Rev. Lett.* **95** 127205

[23] Boninsegni M and Prokofév N 2005 *Phys. Rev. Lett.* **95** 237204

[24] Wang F, Pollmann F and Vishwanath A 2009 *Phys. Rev. Lett.* **102** 017203

[25] Heidarian D and Paramekanti A 2010 *Phys. Rev. Lett.* **104** 015301

[26] Danshita I and Sá de Melo C A R 2009 *Phys. Rev. Lett.* **103** 225301

[27] Ye J W 2006 *Phys. Rev. Lett.* **97** 125302

[28] Kim E and Chan M H W 2004 *Nature* **427** 225

[29] Kim D Y and Chan M H W 2012 *Phys. Rev. Lett.* **109** 155301

[30] Ng K K, Chen Y C and Tzeng Y C 2010 *J. Phys.: Condens. Matter* **22** 185601

[31] Wang Y M and Liang J Q 2012 *Chin. Phys. B* **21** 060305

[32] Matsuda H and Tsuneto T 1970 *Prog. Theor. Phys.* **46** 411

[33] Metcalf B D 1974 *Phys. Lett. A* **46** 325

[34] Gan J Y, Zhang F C and Su Z B 2003 *Phy. Rev. B* **67** 144427

[35] Sage J M, Sainis S, Bergeman T and DeMille D 2005 *Phys. Rev. Lett.* **94** 203001

[36] Rieger T, Junglen T, Rangwala S A, Pinkse P W H and Rempe G 2005 *Phys. Rev. Lett.* **95** 173002

[37] Wang D, Qi J, Stone M F, Nikolayeva O, Wang H, Hattaway B, Gensemer S D, Gould P L, Eyler E E and Stwalley W C 2004 *Phys. Rev. Lett.* **93** 243005

[38] van de Meerakker S Y T, Smeets P H M, Vanhaecke N, Jongma R T and Meijer G 2005 *Phys. Rev. Lett.* **94** 023004

[39] Pollet L, Picon J D, Büchler H P and Troyer M 2010 *Phys. Rev. Lett.* **104** 125302

[40] Pupillo G, Micheli A, Büchler H P and Zoller P 2008 arXiv: cond-mat 0805.1896

[41] Büchler H P, Demler E, Lukin M, Micheli A, Prokofév N, Pupillo G and Zoller P 2007 *Phys. Rev. Lett.* **98** 060404